Temperature dependent spectroscopic ellipsometry and Raman scattering of $PbTiO_3$-based relaxor ferroelectric single crystals around MPB region

X. L. Zhang,[1] J. J. Zhu,[1] G. S. Xu,[2] J. Z. Zhang,[1] L. P. Xu,[1] Z. G. Hu,[1,*] and J. H. Chu [1]

[1]*Key Laboratory of Polar Materials and Devices, Ministry of Education, Department of Electronic Engineering, East China Normal University, Shanghai 200241, China*
[2]*R&D Center of Synthetic Crystals, Shanghai Institute of Ceramics, Chinese Academy of Sciences, Shanghai 201800, China*

[*]*zghu@ee.ecnu.edu.cn*

Abstract: To discover intrinsic relationship between optical bandgap and structural transformations in relaxor ferroelectric single crystals, electronic band structures and dielectric functions of xPb($In_{1/2}Nb_{1/2}$)O_3-$(1-x-y)$Pb($Mg_{1/3}Nb_{2/3}$)O_3-$y$$PbTiO_3$ single crystals (x∼0.27-0.28, y∼0.29-0.35) around morphotropic phase boundary have been investigated by variable-temperature (200-750 K) spectroscopic ellipsometry. It was found that the discontinuous evolution from the second derivative of dielectric functions corresponds to structural transformation patterns. Using the SCP (standard critical point) model, four typical interband transitions (E_a∼2.8 eV, E_b∼3.6 eV, E_c∼4.6 eV, and E_d∼5.4 eV) can be uniquely assigned. These interband transitions are mainly attributed to the contributions from B-O bonds and multiphase coexistence. Furthermore, a modified phase diagram based on interband transition variations with the temperature and PT composition for PIMN-PT crystals was provided. In order to verify the accuracy of phase transition temperature, temperature-dependent low-wavenumber Raman scattering was used as a support. The present results provide important supports for the theoretical model, which establish a quantitative relationship between the electronic transition and structural transformation for ferroelectric oxides.

OCIS codes: (240.0240) Optics at surfaces; (160.4760) Optical properties; (130.2260) Ferroelectrics; (120.6200) Spectrometers and spectroscopic instrumentation.

References and links

1. S.-E. Park and T. R. Shrout, "Ultrahigh strain and piezoelectric behavior in relaxor based ferroelectric single crystals," J. Appl. Phys. **82**, 1804–1811 (1997).
2. S. Kamba and J. Petzelt, *in Piezoelectric Single Crystals and Their Application*, edited by S. Trolier-McKinstry, L. E. Cross and Y. Yamashita (Penn State University, 2004).
3. J. F. Scott, "Applications of Modern Ferroelectrics," Science **315**, 954–959 (2007).
4. M. Suewattana and D. J. Singh, "Electronic structure and lattice distortions in $PbMg_{1/3}Nb_{2/3}O_3$ studied with density functional theory using the linearized augmented plane-wave method," Phys. Rev. B **73**, 224105 (2006).

#247110 Received 30 Jul 2015; revised 23 Sep 2015; accepted 1 Oct 2015; published 12 Oct 2015

5. D. W. Wang, M. S. Cao, and S. J. Zhang, "Phase diagram and properties of $Pb(In_{1/2}Nb_{1/2})O_3$-$Pb(Mg_{1/3}Nb_{2/3})O_3$-$PbTiO_3$ polycrystalline ceramics," J. Eur. Ceram. Soc. **32**, 433–439 (2012).
6. H. Zou, J. Li, X. Wang, D. Peng, Y. Li, and X. Yao, "Color-tunable upconversion emission and optical temperature sensing behaviour in Er-Yb-Mo codoped $Bi_7Ti_4NbO_{21}$ multifunctional ferroelectric oxide," Opt. Mater. Express **4**, 1545–1554 (2014).
7. X. L. Zhang, J. J. Zhu, G. S. Xu, J. Z. Zhang, Z. G. Hu, and J. H. Chu, "Photoluminescence study on polar nanoregions and structural variations in $Pb(Mg_{1/3}Nb_{2/3})O_3$-$PbTiO_3$ single crystals," Opt. Express **22**, 21903–21911 (2014).
8. Jr. G. A. Rossetti, G. Popov, E. Zlotnikov, and N. Yao, "Domain structures and nonlinear mechanical deformation of soft $Pb(Zr_xTi_{1-x})O_3$ (PZT) piezoelectric ceramic fibers," Mater. Sci. Eng. A **433**, 124–132 (2006).
9. Z. G. Ye, "High-performance piezoelectric single crystals of complex perovskite solid solutions," MRS Bullentin **34**, 277–283 (2009).
10. M. Ahart, M. Somayazulu, R. E. Cohen, P. Ganesh, P. Dera, H. K. Mao, R. J. Hemley, Y. Ren, P. Liermann, and Z. G. Wu, "Origin of morphotropic phase boundaries in ferroelectrics," Nature **451**, 545–548 (2008).
11. N. Zhang, H. Yokota, A. M. Glazer, Z. Ren, D. A. Keen, D. S. Keeble, P. A. Thomoas, and Z.-G. Ye, "The missing boundary in the phase diagram of $PbZr_{1-x}Ti_xO_3$," Nat. Commun. **5**, 5231 (2014).
12. M. Rössle, C. N. Wang, P. Marsik, M. Yazdi-Rizi, K. W. Kin, A. Dubroka, I. Marozau, C. W. Schneider, J. Humlicek, D. Baeriswyl, and C. Bernhard, "Optical probe of ferroelectric order in bulk and thin-film perovskite titanates," Phys. Rev. B **88**, 104110 (2013).
13. B. Ghebouli, M. Ghebouli, T. Chihi, M. Fatmi, S. Boucetta, and M. Reffas, "First-principles study of structural, elastic, electronic and optical properties of $SrMO_3$ (M=Ti and Sn)," Solid State Commun. **149**, 2244–2249 (2009).
14. X. L. Zhang, Z. G. Hu, G. S. Xu, J. J. Zhu, Y. W. Li, Z. Q. Zhu, and J. H. Chu, "Optical bandgap and phase transition in relaxor ferroelectric $Pb(Mg_{1/3}Nb_{2/3})O_3$-$xPbTiO_3$ single crystals: An inherent relationship," Appl. Phys. Lett. **103**, 051902 (2013).
15. J. J. Zhu, K. Jiang, G. S. Xu, Z. G. Hu, Y. W. Li, Z. Q. Zhu, and J. H. Chu, "Temperature-dependent Raman scattering and multiple phase coexistence in relaxor ferroelectric $Pb(In_{1/2}Nb_{1/2})O_3$-$Pb(Mg_{1/3}Nb_{2/3})O_3$-$PbTiO_3$ single crystals," J. Appl. Phys. **114**, 153508 (2013).
16. Z. H. Duan, Z. G. Hu, K. Jiang, G. S. Wang, X. L. Dong, and J. H. Chu, "Temperature-dependent dielectric functions and interband critical points of relaxor lead hafnate-modified $PbSc_{1/2}Ta_{1/2}O_3$ ferroelectric ceramics by spectroscopic ellipsometry," Appl. Phys. Lett. **102**, 151908 (2013).
17. H. Lee, Y. S. Kang, S. J. Cho, B. Xiao, H. Morkoç, T. D. Kang, G. S. Lee, J. B. Li, S. H. Wei, P. G. Snyder, and J. T. Evans, "Dielectric functions and electronic band structure of lead zirconate titanate thin films," J. Appl. Phys. **98**, 094108 (2005).
18. P. Lautenschlager, M. Garriga, S. Logothetidis, and M. Cardona, "Interband critical points of GaAs and their temperature dependence," Phys. Rev. B **35**, 9174–9189 (1987).
19. H. Frölich, *Theory of Dielectrics* (Clarendon Press, 1949).
20. R. D. King-Smith and D. Vanderbilt, "First-principles investigation of ferroelectricity in perovskite compounds," Phys. Rev. B **49**, 5828–5844 (1994).
21. Z. Zhang, P. Wu, K. P. Ong, L. Lu, and C. Shu, "Electronic properties of A-site substituted lead zirconate titanate: Density functional calculations," Phys. Rev. B **76**, 125102 (2007).
22. G. Kresse and J. Furthmüller, "Efficient iterative schemes for ab initio total-energy calculations using a plane-wave basis set," Phys. Rev. B **54**, 11169–11186 (1996).
23. G. S. Xu, K. Chen, D. F. Yang, and J. B. Li, "Growth and electrical properties of large size $Pb(In_{1/2}Nb_{1/2})O_3$-$Pb(Mg_{1/3}Nb_{2/3})O_3$-$PbTiO_3$ crystals prepared by the vertical Bridgman technique," Appl. Phys. Lett. **90**, 032901 (2007).
24. O. Svitelskiy, J. Toulouse, G. Yong, and Z. -G. Ye, "Polarized Raman study of the phonon dynamics in $Pb(Mg_{1/3}Nb_{2/3})O_3$ crystal," Phys. Rev. B **68**, 104107 (2003).
25. X. Chen, P. P. Jiang, Z. H. Duan, Z. G. Hu, X. F. Chen, G. S. Wang, X. L. Dong, and J. H. Chu, "The A-site driven phase transition procedure of $(Pb_{0.97}La_0.02))(Zr_{0.42}Sn_{0.40}Ti_{0.18})O_3$ ceramics: An evidence from electronic structure variation," Appl. Phys. Lett. **103**, 192910 (2013).
26. E. W. Sun, S. J. Zhang, J. Luo, T. R. Shrout, and W. W. Cao, "Elastic, dielectric, and piezoelectric constants of $Pb(In_{1/2}Nb_{1/2})O_3$-$Pb(Mg_{1/3}Nb_{2/3})O_3$-$PbTiO_3$ single crystal poled along $[011]_c$," Appl. Phys. Lett. **97**, 032902 (2010).
27. S. Zapf, H. S. Jeevan, T. Ivek, F. Pfister, F. Klingert, S. Jiang, D. Wu, P. Gegenwart, R. K. Kremer, and M. Dressel, "$EuFe_2(As_{1-x}P_x)_2$: Reentrant Spin Glass and Superconductivity," Phys. Rev. Lett. **110**, 237002 (2013).
28. J. J. Zhu, J. Z. Zhang, G. S. Xu, X. L. Zhang, Z. G. Hu, and J. H. Chu, "Electronic transitions and dielectric functions of relaxor ferroelectric $Pb(In_{1/2}Nb_{1/2})O_3$-$Pb(Mg_{1/3}Nb_{2/3})O_3$-$PbTiO_3$ single crystals: Temperature dependent spectroscopic study," Appl. Phys. Lett. **104**, 132903 (2014).
29. J. J. Zhu, W. W. Li, G. S. Xu, K. Jiang, Z. G. Hu, and J. H. Chu, "A phenomenological model of electronic band structure in ferroelectric $Pb(In_{1/2}Nb_{1/2})O_3$-$Pb(Mg_{1/3}Nb_{2/3})O_3$-$PbTiO_3$ single crystals around the morphotropic phase boundary determined by temperature-dependent transmittance spectra," Acta Mater. **59**, 6684–

#247110 Received 30 Jul 2015; revised 23 Sep 2015; accepted 1 Oct 2015; published 12 Oct 2015

6690 (2011).
30. B. Noheda, "Structure and high-piezoelectricity in lead oxide solid solutions," Curr. Opin. Solid State Mater. Sci. **6**, 27–34 (2002).
31. T. T. Fang and H. Y. Chung, "Dielectric relaxation behavior of undoped, Ce-, and Cr-doped $Sr_{0.5}Ba_{0.5}Nb_2O_6$ at high temperatures," Appl. Phys. Lett. **94**, 092905 (2009).
32. K. Y. Chan, W. S. Tsang, C. L. Mak, K. H. Wong, and P. M. Hui, "Effects of composition of $PbTiO_3$ on optical properties of (1-x)$Pb(Mg_{1/3}Nb_{2/3})O_3$-x$PbTiO_3$ thin films," Phys. Rev. B **69**, 144111 (2004).
33. W. Zhong and D. Vanderbilt, "Competing Structural Instabilities in Cubic Perovskites," Phys. Rev. Lett. **74**, 2587–2590 (1995).
34. I. MacLaren, R. Villaurrutia, and A. Pel*á*iz-Barranco, "Domain structures and nanostructures in incommensurate antiferroelectric $Pb_xLa_{1-x}(Zr_{0.9}Ti_{0.1})O_3$," J. Appl. Phys. **108**, 034109 (2010).
35. S. G. Choi, J. Hu, L. S. Abdallah, M. Limpinsel, Y. N. Zhang, S. Zollner, R. Q. Wu, and M. Law, "Pseudodielectric function and critical-point energies of iron pyrite," Phys. Rev. B **86**, 115207 (2012).
36. W. Chan, Z. Xu, T. F. Hung, and H. Chen, "Effect of La substitution on phase transitions in lead zirconate stannate titanate (55/35/10) ceramics," J. Appl. Phys. **96**, 6606 (2004).
37. A. S. Mischenko, Q. Zhang, R. W. Whatmore, J. F. Scott, and N. D. Mathur, "Giant electrocaloric effect in the thin film relaxor ferroelectric 0.9$PbMg_{1/3}Nb_{2/3}O_3$C0.1$PbTiO_3$ near room temperature," Appl. Phys. Lett. **89**, 242912 (2006).
38. B. Mihailova, B. Maier, C. Paulmann, T. Malcherek, J. Ihringer, M. Gospodinov, R. Stosch, B. Güttler, and U. Bismayer, "High-temperature structural transformations in the relaxor ferroelectrics $PbSc_{0.5}Ta_{0.5}O_3$ and $Pb_{0.78}Ba_{0.22}Sc_{0.5}Ta_{0.5}O_3$," Phys. Rev. B **77**, 174106 (2008).

1. Introduction

Relaxor ferroelectrics have been a focus of intense attention in recent years. They can be applied in tunable capacitors, actuators, and electro-optic devices [1–7]. As a fresh member in ferroelectric family, the complex ferroelectric material $Pb(In_{1/2}Nb_{1/2})O_3$-$Pb(Mg_{1/3}Nb_{2/3})O_3$-$PbTiO_3$ (PIMN-PT) single crystal attracts more and more attention because it has a higher dielectric permittivity than that of conventional $Pb(Zr_{1-x}Ti_x)O_3$ (PZT) [8] and expands more temperature application range than that of $Pb(Mg_{1/3}Nb_{2/3})O_3$-$PbTiO_3$ (PMN-PT) [9]. This crystal occupies a variety of structures with different compositions and temperatures, especially in morphotropic phase boundary (MPB) region, where an intermediate phase or coexistence of multiple phases was found [10]. This material belongs to the class of crystal structures known as perovskites with formula ABO_3. The A cation occupies the space between the octahedra while the B cation is at the center of the octahedra [11]. The bandgap variations for ferroelectric and dielectric systems are usually explained by the following factors: (i) thermal expansion of lattice, (ii) renormalization of the band structure by electron-phonon interaction, and (iii) phase transitions. To date, extensive experimental studies have supported the notion that the former two factors contribute more, especially in semiconductors [12, 13]. However, there may be different physical mechanisms in relaxor ferroelectrics due to the known phase/structure transitions. Interestingly, we proved that phase transition is always accompanied by significant changes of optical properties for relaxor ferroelectrics [14, 15]. It suggests that there are some physical signals on phase structure from typical spectral analysis. Although the above concept has been widely accepted, the critical issue is to answer the following problems: (i) Is there an intrinsic relationship between electronic structures and different phases? (ii) Is it possible for us to judge phase transitions by solid state spectroscopy?

Complex dielectric function ($\varepsilon=\varepsilon_1+i\varepsilon_2$) is directly related to electronic band structure of materials, which are crucial for the design and optimization of optoelectronic devices [16]. Especially, the imaginary part (ε_2) can reflect the electronic transition information of materials. Compared with other methods, such as nuclear magnetic resonance (NMR), nuclear quadrupole resonance (NQR), bete-detected NMR, and second harmonic generation (SHG), spectroscopic ellipsometry (SE), which is sensitive to single crystals and surfaces, is not only a nondestructive but also a powerful technique to investigate optical properties [17, 18]. SE is regarded as a highly appropriate method to determine dielectric functions of condensed matter materials

#247110 Received 30 Jul 2015; revised 23 Sep 2015; accepted 1 Oct 2015; published 12 Oct 2015

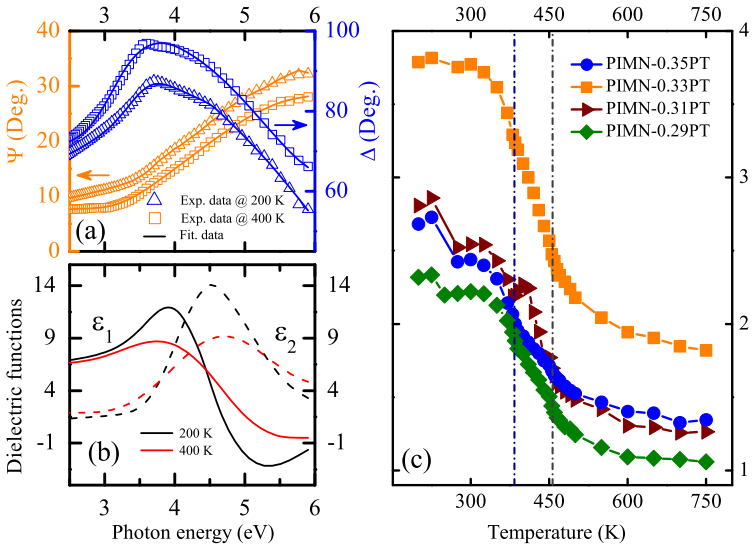

Fig. 1. (a) The experimental data (dots) and calculated curves (lines) of Ψ and Δ at 200 K and 400 K for PIMN-0.33PT single crystal. (b) The real part (ε_1) and imaginary part (ε_2) of numerically inverted complex dielectric functions at 200 K and 400 K. (c) Imaginary parts of dielectric functions for PIMN-PT crystals at the photon energy of 3 eV.

over a wide energy and temperature range. This technique has also been shown essential for investigating optical properties and microstructures of ferroelectrics, which can bring more information on the electron structure of materials and help to better understand the features of chemical bonding and structural transformations. On the other hand, the softening of transverse optic (TO) phonon was predicted by combining the Lyddane-Sachs-Teller (LST) relation with the Curie-Weiss law [19]. According to the prediction, the mode frequency of the TO phonon related to a certain displacive transition becomes zero at the Curie temperature (T_c). That means low-wavenumber Raman scattering (LWRS) technique, which is sensitive to the soft optic phonon, is a good tool in understanding phase transition.

In this article, we have undertaken to develop a scheme with temperature and composition dependence of dielectric functions and phonon Raman scattering of PIMN-PT single crystals by SE and LWRS. We show that interband transitions exhibit anomalous temperature dependence with pronounced changes in the vicinity of ferroelectric transition, which agrees well with previous studies on the phase diagram and theoretical studies of PT based relaxor ferroelectrics by electrical techniques [20–22]. Moreover, the interesting temperature dependence of interband transitions is visible even from the second derivative of ε_2. Correspondingly, a phase diagram based on interband transition variations with the temperature and PT composition was provided. Furthermore, LWRS technique was used as a support to verify the accuracy of phase transition temperature.

2. Experimental details

The *x*PIN-(1-*x*-*y*)PMN-*y*PT single crystals were prepared using a vertical Bridgman technique [23]. The oxide powders with purities better than 99.99%, comprising PbO, In_2O_3, MgO, Nb_2O_5, and TiO_2, were used as starting reagents and mixed. The materials were presynthesized using the two-step Columbite precursor route before being filled into platinum crucibles. PIMN-PT crystals were used as crystal seeds with the diameter size smaller than or equal to

#247110 Received 30 Jul 2015; revised 23 Sep 2015; accepted 1 Oct 2015; published 12 Oct 2015

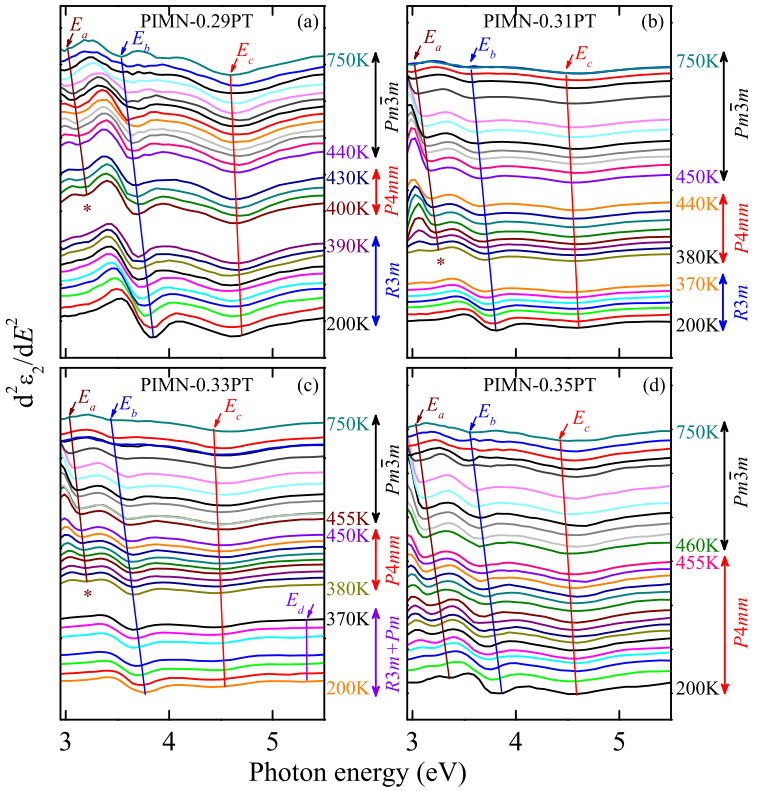

Fig. 2. Temperature dependence of the second derivatives of ε_2 for (a) PIMN-0.29PT, (b) PIMN-0.31PT, (c) PIMN-0.33PT, and (d) PIMN-0.35PT crystals. Note that the solid lines show some significant variation trends to guide the eyes.

the crystal boules. Then, the Pt crucibles were put into alumina crucibles with a supporting setup. The crucible system was driven down through the heat zone at about 1400 °C at a speed of 0.2-0.8 mm/h after socking for more than 10 h. The samples were all cut perpendicular to the <001> direction. Therefore, the effect from the crystal orientation can be ignored. The nominal compositions were $x\sim0.27$-0.28 and $y\sim0.29$-0.35. Detailed X-ray powder diffraction (XRD) information about the specimen could refer to the previous work [15].

Temperature dependent SE experiments were carried out in the photon energy range of 2.5-6 eV (200-500 nm) by a vertical variable-angle near-infrared-ultraviolet spectroscopic ellipsometer (V-VASE by J. A. Woollam Co., Inc.). The data were recorded with the zone average polarizer at an incident angle of 70° and the spectral resolution is set to 2 nm. For variable-temperature measurements, the crystals were mounted into an Instec cell and the temperature can be controlled from 200 to 750 K with the set-point stability of better than 1 K (Janis ST-400). Note that the surface roughness is about 6 nm, which can be derived from atomic force microscopy (AFM) experiment (Bruker Dimension Icon). Temperature dependent low-wavenumber Raman scattering was carried out in the frequency range of 10-400 cm^{-1} by a Jobin-Yvon LabRAM HR 800 UV spectrometer. A 633 nm line of a He-Ne laser was used as the exciting source. For variable-temperature measurements, the crystals were mounted into a Linkam THMSE 600 heating/cooling stage and the temperature can be controlled from 77 to 800 K with the set-point stability of better than 1 K. To get rid of the trivial temperature dependence, all Raman spectra have been divided by the Bose-Einstein occupation number

#247110 Received 30 Jul 2015; revised 23 Sep 2015; accepted 1 Oct 2015; published 12 Oct 2015

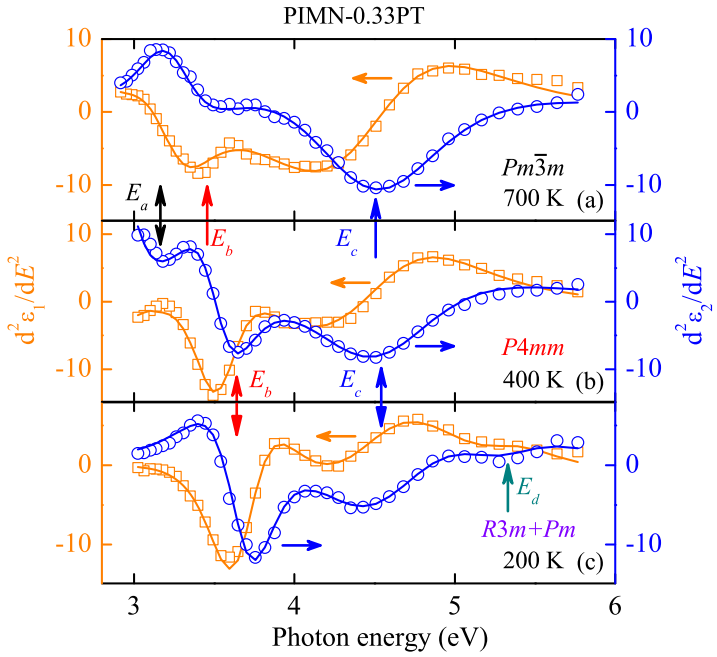

Fig. 3. Experimental (dots) and the best-fit (solid lines) second derivatives of ε at (a) 700 K (in *C* phase), (b) 400 K (in *T* phase), and (c) 200 K (in MPB region) for PIMN-0.33PT crystal, respectively.

$n(\omega)+1=1/[1\text{-}\exp(-\hbar\omega/k_BT)]$ ($\hbar$ and k_B are Planck constant and Boltzmann constant, respectively) [24].

3. Results and discussion

3.1. *Ellipsometric spectra*

The optical behaviors of all single crystals with different phases were investigated by spectroscopic ellipsometry based on the reflectance configuration. It is a sensitive and nondestructive optical technique, which measures the relative changes in the amplitude and phase of particular directions' polarized lights upon oblique reflection from the sample surface. As we know, the complex dielectric functions are intrinsically associated with energy band structures and electronic transitions. Moreover, some obvious variations of optical constants can be caused by structural changes during phase transformations. In order to extract the optical bandgap, dielectric functions, and thickness of surface roughness of the crystals, a three-layer model (air/surface roughness/crystal) was applied in this study. The surface roughness layer was modeled by Brüggeman effective medium approximation; the complex dielectric functions of all crystals were estimated from parametric oscillators Psemi-M0 and Psemi-M3 [25]. The three-layer model is in good agreement with Ψ and Δ, as revealed in Fig. 1(a). The fitted thickness of the roughness layer is 8±3 nm. Given the accurate thickness of the roughness layer, numerically inverted complex dielectric functions of all crystals at every temperature was calculated from the original experimental data. Numerically inverted complex dielectric functions at 200 K and 400 K are shown in Fig. 1(b). The further studies are based on these numerically inverted complex dielectric functions. Figure 1(c) shows the imaginary parts of ε_2 at 3 eV for PIMN-PT single crystals from 200 to 750 K. Note that the temperature range contains all well-

#247110 Received 30 Jul 2015; revised 23 Sep 2015; accepted 1 Oct 2015; published 12 Oct 2015

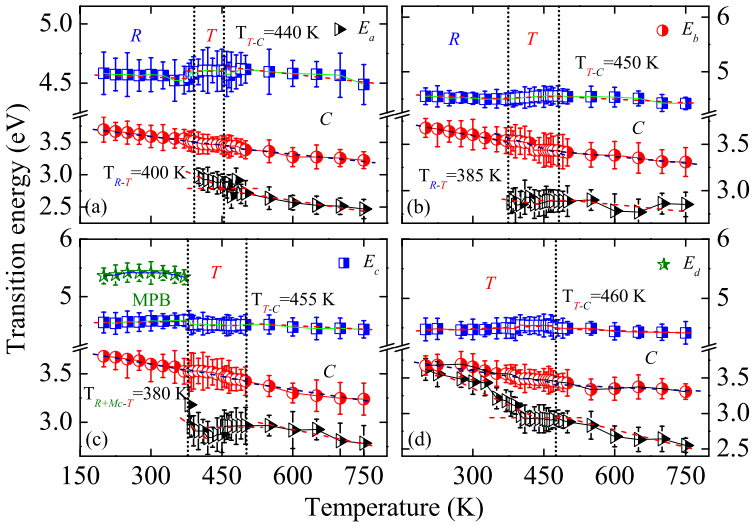

Fig. 4. Temperature dependence of the interband critical point energies for (a) PIMN-0.29PT, (b) PIMN-0.31PT, (c) PIMN-0.33PT, and (d) PIMN-0.35PT crystals, respectively. The dot lines are applied to guide the eyes and indicate anomaly behavior.

known phase transition temperatures of PIMN-PT crystals. It is evident that the intensity of ε_2 located around 3 eV increases with decreasing temperature. As we know, the B-site atom arrangement can be related to the electronic band structure and the parameter ε_2. Also, the lattice expansion and the oxygen vacancies mostly affect the formation of band structures and induce the decrement of ε_2. The imaginary part ε_2 keeps stable at both high and low temperature regions, while it shows a downward trend between 380 and 455 K. These characteristic temperature points are consistent with T_{R-T}=391 K [where a rhombohedral-tetragonal (*R*-*T*) phase transition takes place] and T_c=465 K (Curie temperature) for PIMN-0.32PT crystal measured by dielectric spectroscopy [26]. The conversion process from near constant to increment appears around 380 K and then returns to near constant around 455 K, which can be ascribed to the enhanced correlations between polar nanoregions or associated with the occurrence of polar-cluster coupling. Note that ε_2 of PIMN-0.33PT, which characterizes the absorption, is the largest among all compositions. These anomalies are probably due to disordered structure near the MPB region, which can increase the optical absorption.

The second derivatives of ε_2 for the PIMN-PT crystals at various temperatures are shown in Fig. 2. Four interband transitions can be unambiguously observed and the CPs (critical points) are labeled as E_a, E_b, E_c, and E_d in the order of increasing photon energy, respectively. The transition E_a of PIMN-0.29PT, PIMN-0.31PT and PIMN-0.33PT crystals only appears in the temperature region above 380 K, marked as an asterisk in Fig. 2(a-c). However, it always appears for PIMN-0.35PT crystal. With increasing temperature, three CPs show an obvious red shift trend. Note that there is a relatively weak CP near 5.4 eV in the low temperature region for PIMN-0.33PT. Surprisingly, the switching points of characteristic regions determined by these CPs are consistent with phase transition temperature of PIMN-PT [5, 27]. It may provide a direct evidence that the second derivative of ε_2 can clearly distinguish the crystal structure.

3.2. High-energy critical points and structural transformations

To further analyze the fine band structures, the second derivative of dielectric functions ($d^2\varepsilon/dE^2$) can be calculated. A line-shape analysis with SCP model was performed, which

#247110 Received 30 Jul 2015; revised 23 Sep 2015; accepted 1 Oct 2015; published 12 Oct 2015

Table 1. **The SCP model parameters for PIMN-PT single crystals are extracted from fitting the second derivatives of dielectric functions. Note that the label "-" means that the corresponding transition does not exist at the temperature. Note that the CP E_d of PIMN-0.33PT at 200 K is appended below the CP E_c of PIMN-0.33PT at 200 K. The 95% reliability of the fitting parameters is given in parentheses.**

		E_a				E_b				E_c			
PTO	Temp.	A_0	ϕ_0	E_0	Γ_0	A_1	ϕ_1	E_1	Γ_1	A_2	ϕ_2	E_2	Γ_2
x	(K)	(eV)	(deg.)	(eV)	(eV)	(eV)	(deg.)	(eV)	(eV)	(eV)	(deg.)	(eV)	(eV)
0.29	200	–	–	–	–	1.24 (0.11)	38.7 (2.4)	3.7 (0.3)	0.31 (0.03)	8.38 (0.67)	39.9 (2.8)	4.6 (0.4)	0.87 (0.08)
	650	0.37 (0.02)	33.7 (2.0)	2.5 (0.2)	0.17 (0.04)	0.97 (0.08)	37.1 (1.9)	3.3 (0.3)	0.35 (0.02)	11.72 (0.91)	39.8 (3.1)	4.6 (0.3)	0.90 (0.08)
0.31	200	–	–	–	–	1.16 (0.09)	38.9 (3.4)	3.7 (0.2)	0.38 (0.03)	7.33 (0.68)	40.0 (4.1)	4.6 (0.3)	0.87 (0.07)
	650	0.91 (0.09)	35.8 (3.0)	2.4 (0.2)	0.57 (0.04)	0.93 (0.06)	37.2 (3.5)	3.3 (0.3)	0.37 (0.03)	11.22 (0.98)	39.7 (3.5)	4.5 (0.4)	0.95 (0.08)
0.33	200	–	–	–	–	1.09 (0.09)	39.4 (3.3)	3.7 (0.5)	0.37 (0.02)	4.43 (0.43)	40.7 (4.0)	4.6 (0.5)	0.83 (0.07)
									E_d:	0.48 (0.03)	40.8 (3.9)	5.4 (0.5)	0.53 (0.05)
	450	0.13 (0.09)	33.5 (3.2)	2.9 (0.3)	0.11 (0.01)	0.76 (0.06)	38.6 (3.5)	3.5 (0.3)	0.30 (0.02)	9.24 (0.87)	40.1 (4.0)	4.5 (0.4)	0.95 (0.08)
	650	0.26 (0.02)	42.4 (3.6)	2.9 (0.2)	0.43 (0.04)	0.60 (0.07)	37.6 (3.6)	3.3 (0.3)	0.35 (0.02)	10.26 (1.03)	39.8 (3.1)	4.5 (0.4)	0.97 (0.08)
0.35	200	0.50 (0.06)	37.4 (3.5)	3.6 (0.4)	0.35 (0.02)	1.74 (0.15)	39.3 (3.7)	3.7 (0.3)	0.47 (0.03)	7.58 (0.72)	39.6 (3.8)	4.5 (0.5)	0.83 (0.07)
	650	0.16 (0.01)	42.9 (4.2)	2.6 (0.2)	0.14 (0.01)	0.94 (0.08)	38.2 (3.9)	3.4 (0.3)	0.43 (0.04)	11.27 (1.22)	39.5 (3.6)	4.4 (0.4)	0.95 (0.09)

has been successfully applied in semiconductors and ferroelectric materials. Compared to other dispersion models, the SCP model shows more advantages in connecting phase transitions and optical bandgap. The SCP expression can be written as the following [18]:

$$\frac{d^2\varepsilon}{dE^2} = \begin{cases} n(n-1)A_m e^{i\phi_m}(E - E_m + i\Gamma_m)^{n-2} & n \neq 0, \\ A_m e^{i\phi_m}(E - E_m + i\Gamma_m)^{-2} & n = 0. \end{cases} \quad (1)$$

Here, A_m, E_m, Γ_m, and ϕ_m in order is the mth amplitude, threshold energy, broadening, and excitonic phase angle, respectively. The exponent n has the value of $-\frac{1}{2}$, 0, $\frac{1}{2}$, and -1, corresponding to the one-dimensional (1D), 2D, 3D, and excitonic CPs, respectively. For our case of bulk material, n=$\frac{1}{2}$. Figure 3 displays the experimental and best-fit second derivatives of dielectric functions at 200 K, 400 K, and 700 K for PIN-PMN-0.33PT crystal, respectively. Correspondingly, the fitting parameter values of SCP model are listed in Table I.

The temperature dependence of fitted CPs is displayed in Fig. 4. As compared to the data derived from electrical experiments, four typical CPs present obvious characteristics for the crystals with different phases. Note that all results have been recorded from single crystal, which cannot be sensitive to the domain variations. That means the temperature changing and interband transitions originate from band structure variations across different phases. Interestingly, it was found that E_d is the characteristic CP for the MPB region because it disappears at the corresponding temperature point. As the temperature increases, PIMN-0.33PT crystal near the MPB region exhibits a monoclinic-tetragonal (M_c-T) phase transition [23]. The temperature, at which E_d disappears while E_a appears, is taken as an assignment to determine T_{Mc-T}=380 K

#247110 Received 30 Jul 2015; revised 23 Sep 2015; accepted 1 Oct 2015; published 12 Oct 2015

[where a M_c-T phase transition takes place]. The parameter E_a is the characteristic CP for the T phase and C phase (cubic phase), which is sensitive to the T-C phase transition. When the T-C phase transformation occurs, the transitions E_b and E_c exhibit significant changes, as shown in Fig. 4. It is obvious that the slop of E_a in the T phase is larger than that in the C phase while it remains nearly constant at the temperature when the T-C transition occurs. In addition, the appearance of E_a implies a rhombohedral-tetragonal (R-T) transition. Note that the interband energies in high temperature region consist well with the interband energies investigated by temperature dependent transmittance and reflectance spectra [28].

When compared to other optical parameters, high-energy critical points can more convincingly identify phase transitions. As we know, low-energy electronic transitions and phonon vibrations are often used to determine structural transformations in materials. However, this kind of changes is always very slight and unstable due to the common sense that particles within material are always in a state of dynamic equilibrium and this type of experiments is often with relatively lower repeatability. Furthermore, results are often obtained through indirect characterization with these techniques. Figure 4 shows a clear corresponding relationship between high-energy critical points and lattice structures. Phase transitions can be undoubtedly judged with emergence or disappearance of typical CPs.

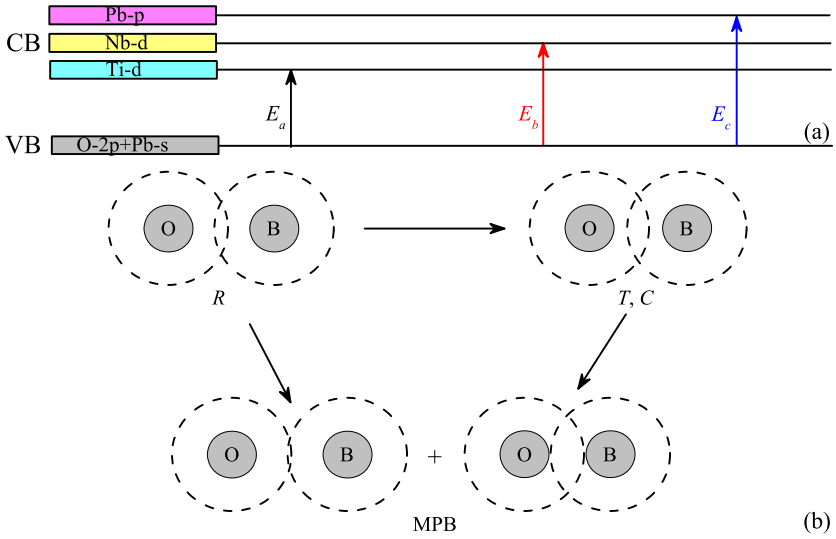

Fig. 5. (a) The assignments for critical point energies E_a, E_b and E_c of PIMNT single crystals. (b) A diagram describes the degree of B-O hybridization in each phase region. Note that the weaker hybridized B-O bond leads to higher-lying interband energy E_d.

3.3. Interband transitions and phase diagram

The parameters E_a and E_b are the lowest transitions among all CPs and their values are consistent with the bandgap energy of PIMN-PT single crystals [29]. It was reported that the changes in B-site have less influence on the bandgap structure when the A-site maintains a constant atom. [20] Therefore, there are slight differences between the bandgap structure of PMN, PZT, PT and PIMN-PT systems [4, 17, 20–22]. It is commonly believed that the BO_6 octahedron building block determines the basic energy level of PIMN-xPT single crystals. The B-cation d

#247110 Received 30 Jul 2015; revised 23 Sep 2015; accepted 1 Oct 2015; published 12 Oct 2015

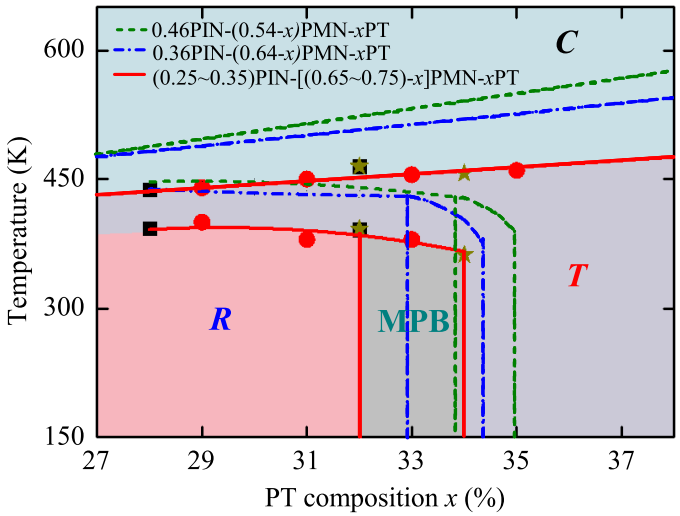

Fig. 6. A phase diagram is based on analysis of the interband critical point variation with the temperature and PT composition. The solid lines indicate the phase transition boundary derived from the present work while the dashed lines are taken from previous study [5]. Note that the shaded area indicates the MPB region determined from the present SE technique.

orbitals associated with its octahedron govern the lower lying conduction bands (CBs) while the O-2*p* and its octahedron determine the upper valence bands (VBs). Other ions in the structure contribute to the higher-lying conduction band, which have tiny effects on the fundamental absorption edge [14]. $PbTiO_3$ is of three transitions (2.8 eV, 4 eV, and 5 eV), [17, 22] among which the lower two transitions are from the O-2*p* to Ti-*d*. It is consistent with the transition energy between the O-2*p* to Ti-*d* of PZT [21]. A higher transition is from the O-2*p* and Pb-*s* to Pb-*p*. These transitions are corresponding to the assigned E_a, E_b and E_c. Moreover, it was reported that energy of transitions from O-2*p* and Pb-*s* to Nb-*d* is closer to E_a and E_b while transitions to Pb-*p* are similar to E_c for PMN system [4]. From the point of view on electronic density of state, energy of Pb-*p* is 1 eV larger than that of Nb-*d* [4]. Therefore, it is reasonable to conclude that E_a and E_b corresponds to transitions from O-2*p* and Pb-*s* to Ti-*d* and Nb-*d*, respectively. On the other hand, for PT-containing ABO_3 perovskite relaxor ferroelectrics, the PT poor ends are always located in the *R* phase region, while the PT rich ends are located in the *T* phase region. It can be determined that transition from O-2*p* to Ti-*d* has larger contribution to E_a because there is no E_a transition in the *R* phase region. Similarly, transition from O-2*p* and Pb-*s* to Nb-*d* has larger contribution to E_b. Figure 5(a) presents a schematic view of the origin for the above interband transitions. The larger transition energy of E_d is probably due to the weaken of Ti-O hybridization and Nb-O hybridization induced by coexistence of multiphase in the MPB region, as shown in Fig. 5(b).

Lattice structure, electronic bandgap, and phase structure are ideally associated by optical parameters in this work. It means that the microcosmic mechanism can be understand with the macroscopical phenomena in an nondestructive way. For example, evolution of electronic bandgap in PIMN-0.33PT can be detected with Fig. 4(c). Crystal is in *C* phase region above 455 K and transitions from O-2*p*+Pb-*s* to Ti-*d*, Nb-*d*, and Pb-*p* are permitted. With decreasing temperature, bond length of lattice changes and this lead to a lower B-O hybridization. Therefore, all electronic transitions take a positive trend and the crystal step into T phase region.

#247110 Received 30 Jul 2015; revised 23 Sep 2015; accepted 1 Oct 2015; published 12 Oct 2015

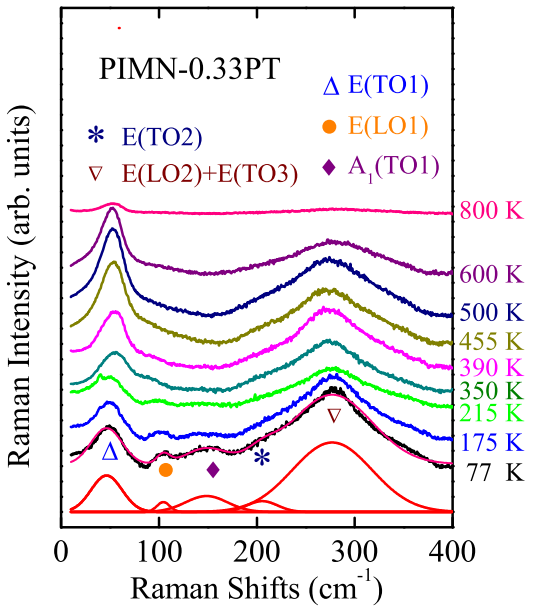

Fig. 7. Temperature dependent Raman spectra of PIMN-0.33PT single crystal, with the Lorentzian-shaped spectral deconvolution at 77 K.

With further decreasing temperature, bond angles of lattice begin to change and this lead to the disappearance of E_a. Here, the crystal get into MPB region with coexistence of multiple phases. Degree of hybridization in each phase of MPB is not unified. Some extreme high bond angles produce extreme low B-O hybridization which can be characterized by E_d. That means the appearance of E_d indicates the MPB region.

Figure 6 presents a schematic phase diagram for relaxor ferroelectric PIMN-PT crystals. The round dots are derived from phase transition temperature in Fig. 4. With polynomial fitting, the boundary lines between phases are plotted which are consistent well with previous study as plotted with stars and rectangles [23]. As can be seen, the *R* phase locates in the region with low PT composition while the *T* phase locates in the PT rich ends. Phase transition process is often accompanied by an intermediate phase or mixed phases. M_c phase is the intermediate phase between *T* and *R* phase, which can coexist with the *R* or *T* phase. The M_c phase was found to be a slightly distorted orthorhombic phase and it is proper to consider the M_c phase as a quasiorthorhombic phase [30]. The broadening of the phase transition may be due to structural disorder and compositional fluctuation in the solid solution [31]. Transition energy between optical bandgap in the *R* phase region is always higher than that in the *T* phase region and *C* phase region for ABO_3-type perovskite relaxor ferroelectrics [14, 32]. This is consistent well with the conclusions that a weaker B-O hybridization is easier to occur in the *R* phase. From Fig. 6, the PIN composition can determine the position of MPB region and transition temperature of PIMN-PT [5]. The MPB region is closer to PT rich ends with increasing the PIN composition. Note that MPB is a multiphase region with a number of disorder and also an instability structure region. Instabilities of perovskites can often be understood in terms of ionic size effects, especially in terms of tolerance factors [33]. Indium atom is a large size atom, as compared with Ti atom and Nb atom and its injection can reduce structure stability of the material. This leads to deviation of MPB region with the PIN composition. Therefore, the phase diagram offers a direct observation on relationships between optical properties and phase transitions.

#247110 Received 30 Jul 2015; revised 23 Sep 2015; accepted 1 Oct 2015; published 12 Oct 2015

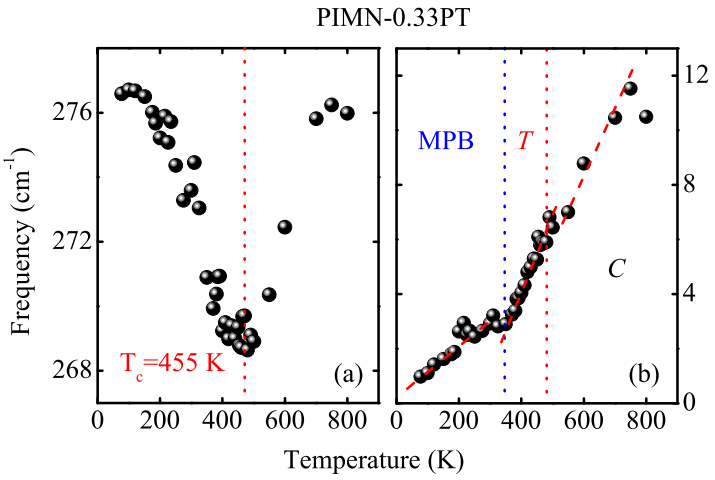

Fig. 8. (a) Temperature dependent E(LO2)+E(TO3) mode for PIMN-0.33PT crystal. (b) The intensity ratio between E(TO1) mode and E(LO2)+E(TO3) as a function of temperature for PIMN-0.33PT crystal. Note that all data are divided into different phase regions with dot lines.

3.4. Low-wavenumber Raman modes

To confirm the results derived from the SE spectra, the temperature dependent Raman scattering of PIMN-PT are investigated. For example, LWRS spectra of PIMN-0.33PT crystal at various temperatures are shown in Fig. 7, as well as the Lorentzian-shaped deconvolution 77 K. Intense measurements show that phonon softening and associated lattice dynamics in ABO_3-type ferroelectric perovskites vary obviously when structural transformations occur [34–38]. Therefore, LWRS technique, which is sensitive to low-frequency excitations close to the intense Rayleigh line, was used to verify phase transition temperatures in phase diagram. Five modes can be unambiguously observed. They are labeled as E(TO1) (50 cm^{-1}) mode, E(LO1) (100 cm^{-1}) mode, A_1(TO1) (130 cm^{-1}) mode, E(TO2) (200 cm^{-1}) mode, and E(LO2)+E(TO3) (280 cm^{-1}) mode according to positions of these Raman peaks. In the high temperature region (above T_c), PIMN-PT crystal is located in *C* phase region. Only E(TO1), E(LO1), and E(LO2)+E(TO3) modes can be detected. With decreasing temperature, obvious weakening trends for E(TO1) mode are observed. Meanwhile, the red shifts take place for E(LO2)+E(TO3) modes. However, these modes present blue shifts at T_c (∼455 K). The variation indicates a cubic-tetragonal (C-T) phase transition. The parameter T_c presents an increasing trend for PIMN-PT crystals with increasing PT composition. The A_1(TO1) and E(TO2) modes appear with a further cooling. These modes are sensitive to lattice distortion and their appearances indicate the co-existence of multi-phase [15].

Figure 8 presents direct relationships between structure transitions and phonon Raman modes. The well-fitted E(LO2)+E(TO3) (275 cm^{-1}) mode with the temperature is shown in Fig. 8(a). This mode presents an overall negative trend in low temperature region and a positive trend in high temperature region. Note that the minimum frequency value of this mode consists well with T_c in phase diagram. Furthermore, obviously competitive relationship can be found between intensity of E(TO1) mode and intensity of E(LO2)+E(TO3) mode [$I_{E(TO1)}/I_{E(LO2)+E(TO3)}$], as presented in Fig. 7(b). The ratio is generally a positive trend and three main regions can be discerned by the slopes. These interrupts of slope give evidence for changes of structural variations [23]. Interestingly, we find that these temperatures consist

#247110 Received 30 Jul 2015; revised 23 Sep 2015; accepted 1 Oct 2015; published 12 Oct 2015

well with both MPB-*T* phase transition temperature and *T*-*C* phase transition temperature for PIMN-0.33PT crystal.

4. Conclusions

In summary, temperature and composition dependence of electronic transitions and phonon Raman scattering of PIMN-PT single crystals have been investigated using spectroscopy ellipsometry and low-wavenumber Raman scattering. Compared to previous study, this research is more systematic and more apparent changes can be observed in both origin data and fitted data. We believe that such significant changes on spectra could be the general patterns and it is feasible to identify the phase structure. A modified phase diagram for PIMN-PT crystals has been provided. It plays an important role in understanding the relationships between optical bandgap and phase structure.

Acknowledgments

This work was financially supported by Major State Basic Research Development Program of China (Grant Nos. 2011CB922200 and 2013CB922300), Natural Science Foundation of China (Grant Nos. 11374097 and 61376129), Projects of Science and Technology Commission of Shanghai Municipality (Grant Nos. 15JC1401600, 14XD1401500, 13JC1402100, and 13JC1404200), and the Program for Professor of Special Appointment (Eastern Scholar) at Shanghai Institutions of Higher Learning.

#247110 Received 30 Jul 2015; revised 23 Sep 2015; accepted 1 Oct 2015; published 12 Oct 2015